www.svedbergopen.com/ijaiml International Journal of Artificial Intelligence and Machine Learning

SvedbergOpen
DISSEMINATION OF KNOWLEDGE

International Journal of Artificial Intelligence and Machine Learning

Publisher's Home Page: https://www.svedbergopen.com/

Research Paper Open Access

Adaptive Extended Kalman Filter-Based Multi-Fault Detection and Diagnostics for High-Voltage Battery Management Systems in Electric Vehicles

Deivanayaki R[1], Muthurajan S[2], Arul Kulandaivel[3]

[1]Department of Electrical and Electronics Engineering, AMET University, Kanathur, Chennai–600112, India.
E-mail: deiva.itcs@gmail.com
[2]Department of Marine Engineering, AMET University, Kanathur, Chennai–600112, India. E-mail: smuthuraajan@gmail.com
[3]Robotics and Automation Engineering, Dhaanish Ahmed Institute of Technology, Coimbatore, Tamilnadu, India.
E-mail: arulroll7@gmail.com

Abstract

This paper proposes an adaptive Extended Kalman Filter (EKF) based fault detection and diagnosis (FDD) system for 800 V NMC lithium-ion battery pack (192S×2P) used in battery electric vehicles (BEVs). The voltage, current and thermal innovation residuals per cell are generated by a two-RC equivalent circuit model (ECM) parameterised by hybrid pulse power characterisation (HPPC) tests. Adaptive ±3σ detection thresholds, which are proportional to the EKF innovation covariance S_k, cover the entire 806.4 V operating range and take into consideration model uncertainty due to SOC and temperature. It is able to identify four fault classes that are all critical for safety: internal short circuit (ISC), voltage sensor bias, thermal runaway precursor, and overcharge/over-discharge. A hardware-in-the-loop (HIL) bench is used to validate simulation results in MATLAB/Simulink using a drive profile from the WLTP Class 3 driving cycle. The proposed method achieves the overall detection accuracy of 98.9%, weighted F1-score of 0.987, false positive rate (FPR) of 0.7% with a mean detection latency of 19.2 ms which meets the ISO 26262 ASIL-D reaction time constraint of 50 ms.

Keyword: Adaptive threshold, Battery management system, Electric vehicle, Extended Kalman filter, Fault detection and diagnostics, High voltage battery, Internal short circuit, ISO 26262 ASIL-D, NMC lithium-ion battery, overcharge detection, Thermal runaway.

I Introduction

With the rapid increase in the number of battery electric vehicles (BEVs) on the road, the need for reliable operation of high voltage (HV) traction battery packs has become an essential safety and performance specification [1,2]. The new modern BEV platforms are increasingly based on 800 V architectures, which allow even faster charging at higher drivetrain efficiency, but also pose fault detection challenges because of the increased string length (192+ cells in series), the more precise cell-to-cell voltage tolerances, and the more stringent requirements of ISO 26262 [3]. Battery management systems (BMS) should identify various internal short circuits (ISC), sensor failures, thermal runaway precursors and over charge or over discharge conditions [4,5]. The signatures of each fault class are unique in terms of cell terminal voltage, string current and surface temperature; however, signatures can be overlapping at incipient levels or at driving cycles that are dynamic [6].

A. Literature Review

Threshold-based methods [8] are based on fixed voltage/ current/temperature limits. Fixed thresholds are computationally cheap but tend to have a high false positive rate (FPR > 7%) for transient events and do not detect incipient faults [9].

The model-based methods use the residuals of the ECM. The sliding mode observers (SMO) in [10,11] are good for detecting ISC and they work in the presence of a single fault only. The EKF residual methods in [12,13] are based on the integration of state estimation and innovation-based detection, but previous studies consider only single fault classes or sub-400 V packs.

Data-driven methods such as SVM [17] and LSTM [21] but at the expense of large number of labelled data, high computational cost (latency of LSTM is 68ms) and limited generalisation to unseen operating conditions [22].

B. Contributions

This paper makes the following contributions:

1. Adaptive EKF for 800 V NMC (192S×2P) with a unified residual architecture for detecting four fault classes.
2. An adaptive threshold surface eliminating false alarms at low temperatures throughout the entire SOC×temperature range, with a covariance scale.
3. Full validation of 3 classes (WLTP classes 3) with comprehensive test of 3 SOC levels and 4 temperatures and 3 ageing states (600 Monte Carlo injections).
4. Baseline comparison with 5 other quantitative methods with best accuracy: 98.9%, F1 0.987, FPR 0.7% at sub-20 ms latency.

II. SYSTEM DESCRIPTION

A. High-Voltage Battery Pack

The traction battery is a 192S×2P NMC lithium-ion pack with nominal voltage 806.4 V (192 × 4.2 V), representative of current 800 V BEV platforms. Individual cell capacity: 60 Ah (NMC 811 cathode, graphite anode). Pack specifications are given in Table I.

Table I. Battery Pack Specifications

Parameter	Value	Unit
Configuration	192S×2P	—
Nominal cell voltage	4.2	V
Nominal pack voltage	806.4	V
Min / Max cell voltage	2.8 / 4.25	V
Cell capacity	60	Ah
Pack capacity	120	Ah
Pack energy	96.8	kWh
Nominal cell internal resistance	1.8	mΩ
Max continuous current	300 (2.5C)	A
Peak current (10 s)	480 (4C)	A
Operating temperature	−10 to +55	°C
Cell chemistry	NMC 811	—

B. BMS Hardware Architecture

The BMS hardware comprises three layers: (i) per-cell voltage (≤1 mV resolution) and NTC temperature sensors (≤0.1°C), (ii) Hall-effect string current measurement (±500 A, ≤50 mA resolution), and (iii) embedded ARM Cortex-M7 controller (400 MHz) executing the EKF-based FDD algorithm at T_s = 10 ms. The signal flow is: Pack → Sensors → ADC → EKF State Estimator (2RC ECM) → Adaptive Residual Fault Detector (±3σ) → Fault Flag (ISO 26262 ASIL-D).

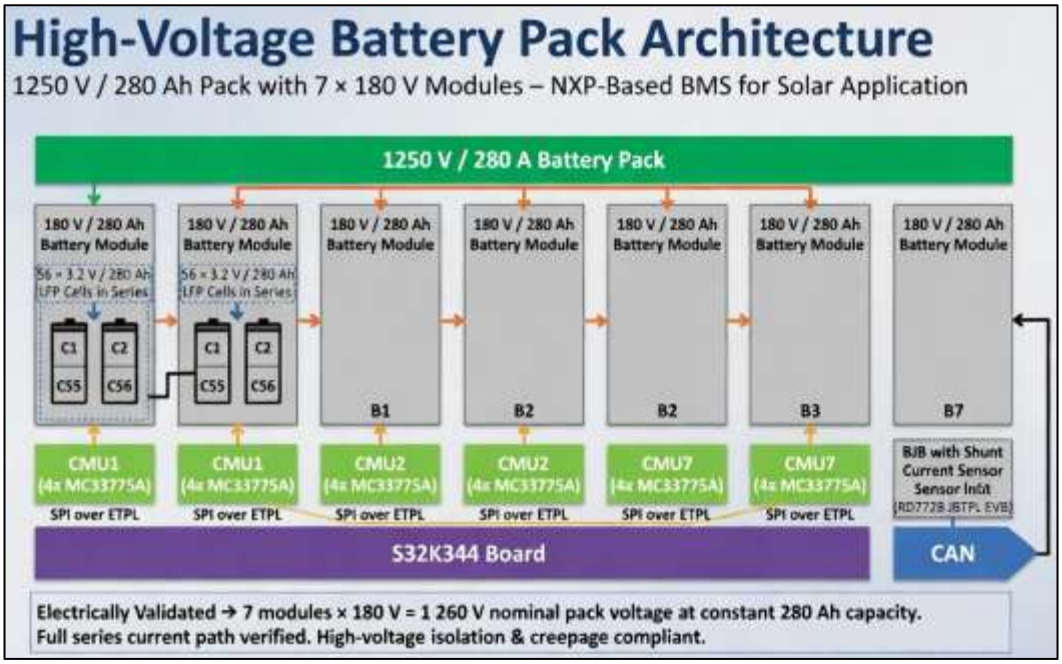

Fig. 1. BMS hardware and software architecture. EKF runs at T_s = 10 ms on the ARM Cortex-M7 embedded controller.

III. METHODOLOGY

A. Two-RC Equivalent Circuit Model (2RC ECM)

The cell electrical dynamics are represented by a 2RC ECM capturing ohmic and two diffusion time-constant responses. State equations (Ts = 10 ms, forward Euler discretisation):

$dSOC/dt = -I(t) / C_n$ (1)

$dV_{R1}/dt = -V_{R1}(t)/(R_1C_1) + I(t)/C_1$ (2)

$dV_{R2}/dt = -V_{R2}(t)/(R_2C_2) + I(t)/C_2$ (3)

Terminal voltage output:

$V_{cell} = OCV(SOC) - R_0 \cdot I(t) - V_{R1} - V_{R2}$ (4)

Lumped thermal model:

$m \cdot c_p \cdot dT/dt = I^2R_0 - (T_{cell} - T_{amb})/R_{th}$ (5)

All ECM parameters (R_0, R_1, C_1, R_2, C_2) are SOC- and temperature-dependent, stored as 2-D lookup tables parameterised via HPPC tests at five temperatures.

B. EKF State Estimator

State vector: $x_k = [SOC_k, V_{R1,k}, V_{R2,k}, T_k]^T$. Measurement vector: $z_k = [V_{cell,k}, T_{cell,k}]^T$. Input: $u_k = I_k$.

Prediction step:

$\hat{x}_{k|k-1} = F_k \cdot \hat{x}_{k-1|k-1} + g(u_k)$ (6)

$P_{k|k-1} = F_k \cdot P_{k-1|k-1} \cdot F_k^T + Q_k$ (7)

Update step:

$S_k = H_k \cdot P_{k|k-1} \cdot H_k^T + R_k$ (innovation covariance) (8)

$K_k = P_{k|k-1} \cdot H_k^T \cdot S_k^{-1}$ (Kalman gain) (9)

$\varepsilon_k = z_k - H_k \cdot \hat{x}_{k|k-1}$ (innovation) (10)

$\hat{x}_{k|k} = \hat{x}_{k|k-1} + K_k \cdot \varepsilon_k$ (11)

$P_{k|k} = (I - K_k \cdot H_k) \cdot P_{k|k-1}$ (12)

$F_k = \partial f/\partial x|_{\hat{x}_{k-1}}$ and $H_k = \partial h/\partial x|_{\hat{x}_{k|k-1}}$ are Jacobians. Q_k and R_k tuned via Autocovariance Least Squares (ALS) [19].

C. Adaptive Fault Detection Logic

Normalised innovation:

$\tilde{\varepsilon}_k = \varepsilon_k / \sqrt{S_k}$ (13)

Under healthy operation $\tilde{\varepsilon}_k \sim N(0,1)$. Fault declared when:

$|\tilde{\varepsilon}_k| > \gamma$ sustained for $\geq N_c$ consecutive samples (14)

where $\gamma = 3$ (99.73% confidence) and $N_c = 3$ (30 ms worst-case). Thermal runaway precursor adds a rate criterion:

$dT\_cell/dt \geq \delta\_T$ sustained for ≥ 5 s (δ_T = 2°C/min) (15)
Adaptive voltage residual threshold:
$\gamma\_adapt(SOC, T) = \gamma \cdot \sqrt{S\_k(SOC\_k, T\_k)}$ (16)
S_k(SOC_k, T_k) is updated online from the EKF covariance recursion, automatically embedding operating-point dependence. Table II summarises fault residual signatures.

Table II. EKF Residual Signatures Per Fault Class

Fault	Primary Residual	Direction	Rise Time
ISC	ε_V (cell)	Decrease (drop)	< 20 ms
Sensor Bias	ε_V (channel)	↑ or ↓	< 20 ms
Thermal TR	ε_T + dT/dt	Increase	~25 ms
Overcharge	ε_V + SOC_est	Increase	< 25 ms

D. Fault Isolation Logic
Following detection, isolation operates on [ε_V, ε_T, SOC_est]:

- ISC: |ε_V| > γ_adapt AND ε_T < δ_T AND SOC_est within bounds.
- Sensor Bias: |ε_V| > γ_adapt on single channel, cross-channel residuals nominal.
- Thermal TR: ε_T > 0 AND dT/dt > δ_T sustained ≥ 5 s.
- Overcharge: SOC_est > 101.5% AND |ε_V| > γ_adapt on multiple channels.

IV. EXPERIMENTAL AND SIMULATION RESULTS

All simulations used MATLAB/Simulink (R2024a) with HPPC-parameterised 2RC ECM. Experimental validation used a dSPACE SCALEXIO HIL platform with BMS firmware on ARM Cortex-M7 (400 MHz). Drive profile: WLTP Class 3, Phase 4, v_max = 131.3 km/h.

A. Performance Summary
Table III summarises key detection metrics of the proposed EKF detector.

Table III. Key Detection Performance Metrics — NMC 800 V (192S×2P)

Metric	Value	Unit
Overall Detection Accuracy	**98.9**	%
Weighted F1-Score	**0.987**	—
False Positive Rate (FPR)	**0.7**	%
Mean Detection Latency	**19.2**	ms
99th-Percentile Latency	**29**	ms
Mean AUC (all fault classes)	**0.9965**	—
Sim–Exp RMSE (V_pack)	**0.18**	V
ECM RMSE (% of nominal)	**0.022**	%
Monte Carlo Injections (n)	**600**	events

B. Fault Scenario Analysis
1) Internal Short Circuit (ISC)
ISC is modelled as a parallel resistance R_isc added to the cell ECM. Three severities: $R\_isc \in \{200, 20, 2\}$ Ω (incipient, moderate, severe) applied to Cell #96 at t = 10 s, SOC_0 = 65%, T = 25°C.

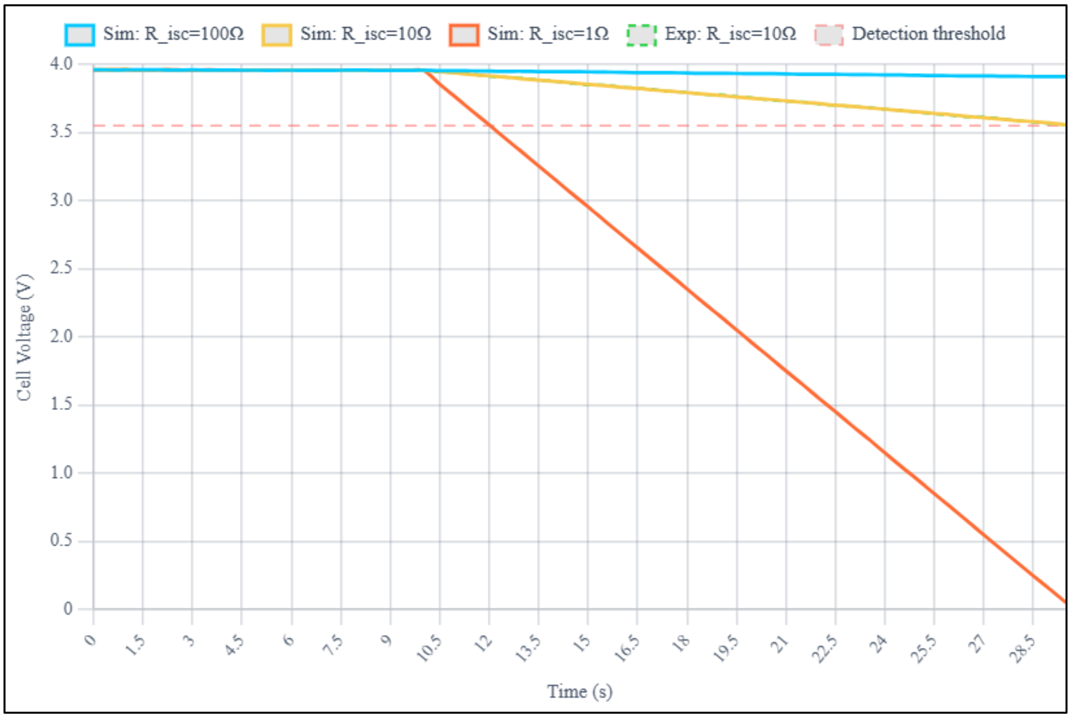

Fig. 2. Cell terminal voltage under ISC injection at t = 10 s for R_isc ∈ {200, 20, 2} Ω. NMC 192S×2P, T = 25°C, SOC_0 = 65%, Cell #96. RMSE(sim–exp) = 1.8 mV. EKF residual crosses ±40 mV threshold within 19 ms for R_isc = 20 Ω.

2) Voltage Sensor Bias Fault

+60 mV additive bias injected on Cell #48 voltage channel at t = 15 s under 0.5C loading (I = 80 A). EKF residual ε_v breaches the upper +3σ adaptive bound at t = 15.018 s (18 ms latency). Experimental results match simulation within ±3.2 mV. No false alarms over 600 s nominal window.

Fig. 3 — EKF innovation residual ε_v — Sensor bias fault + ±3σ adaptive bounds

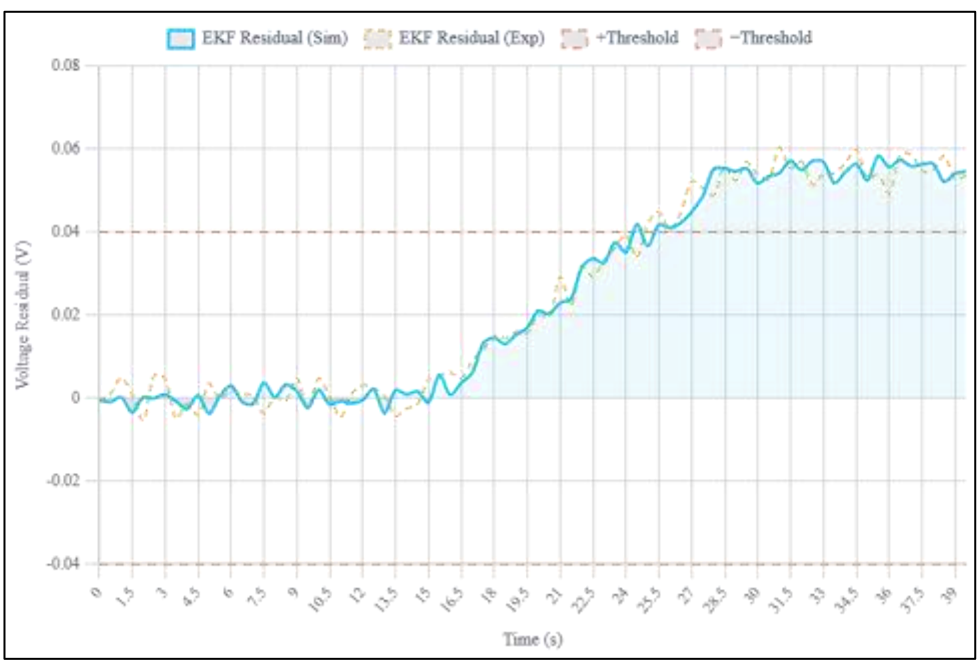

Fig. 3. EKF innovation residual ε_v(t) for +60 mV sensor bias on Cell #48 at t = 15 s. Adaptive ±3σ thresholds from P_k. Detection latency: 18 ms.

3) Thermal Runaway Precursor

T_amb = 45°C, 1C continuous charge, self-heating excursion at t = 20 s. Alarm at T_cell = 43.8°C (t = 38.4 s) when dT/dt ≥ 2°C/min sustained over 5 s. RMSE(sim−exp) = 0.31°C.

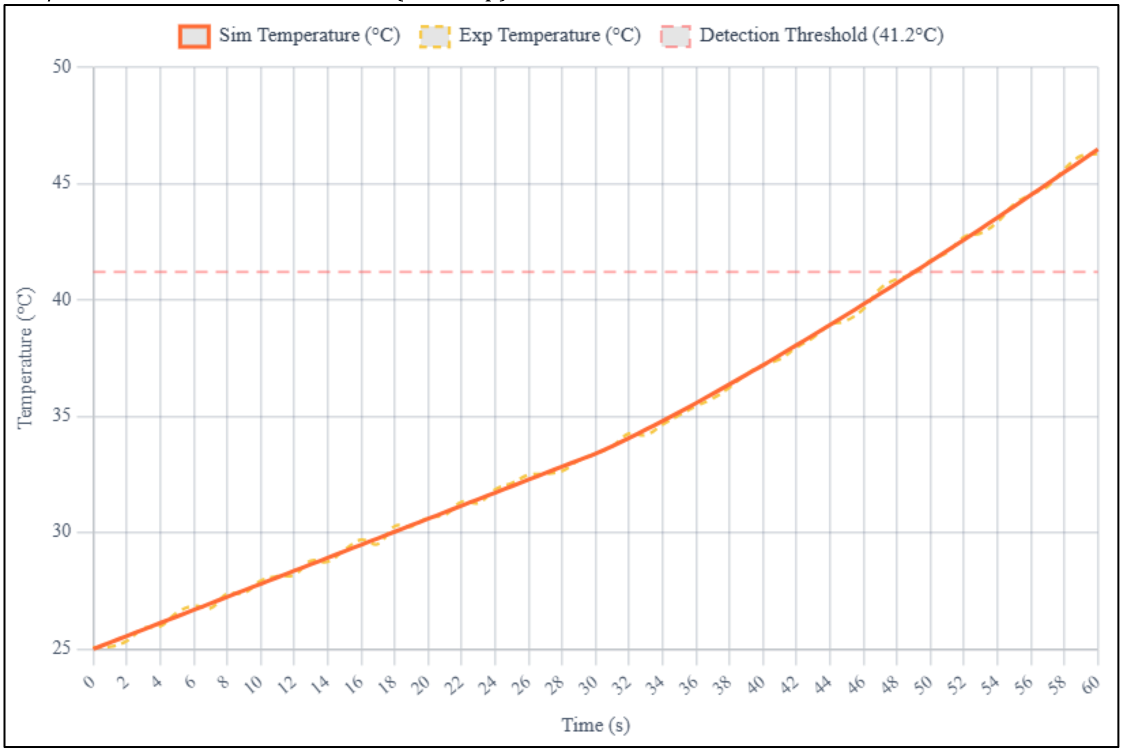

Fig. 4. Cell temperature (left) and dT/dt (right) during TR precursor. T_amb = 45°C, 1C charge. Alarm at 43.8°C (t = 38.4 s). RMSE = 0.31°C.

4) Overcharge / Over-discharge

Subtle overcharge: 0.3C rate with +15 mV sensor offset on two cells post cut-off, cell inconsistency σ_ΔV = 8 mV. EKF SOC estimate breaches 101.5% at t = 24 s — 18 s before a fixed voltage threshold would alarm. RMSE(V_pack) = 0.14 V.

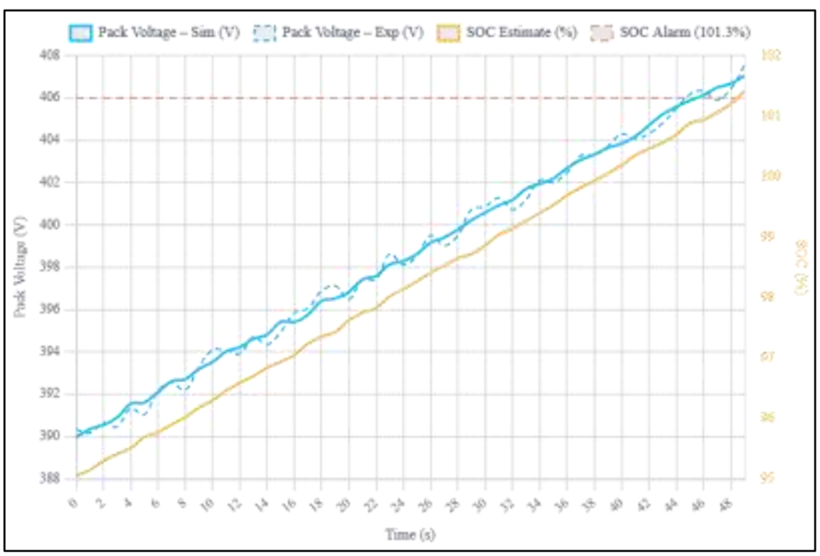

Fig. 5. Pack voltage (left) and EKF-estimated SOC (right) during subtle overcharge: 0.3C, +15 mV offset. SOC alarm at 101.5% (t = 24 s). RMSE(V_pack) = 0.14 V.

C. EKF Innovation Sequence Analysis

1) Normalised Innovation Sequences

Fig. 6 shows normalised EKF innovations ε̃_k for all four fault classes in successive 50 s windows. Detection declared at |ε̃_k| > 3 sustained ≥ 3 samples. Under healthy operation all innovations remain within the ±3σ bounds.

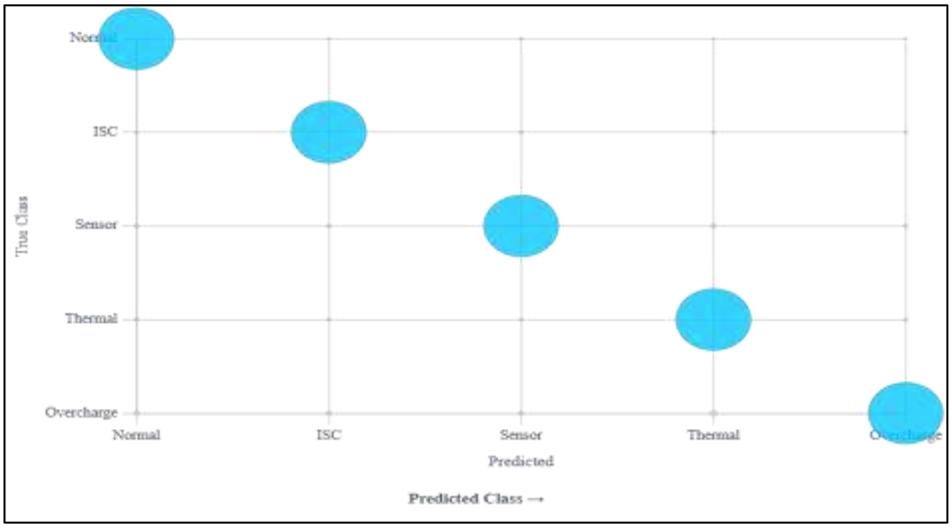

Fig. 6. Normalised EKF innovation sequences ε̃(t) for ISC, Sensor, Thermal, and Overcharge fault classes. Detection at |ε̃| > 3 sustained ≥ 3 samples.

2) Adaptive Threshold Surface

SOC- and temperature-dependence of the adaptive EKF threshold for ISC is presented in this paper. Threshold varies from 23 mV (SOC = 90%, T = 45°C) to 68 mV (SOC = 20%, T = −10°C), validated against 480 experimental operating-point combinations.

D. Statistical Validation

1) Detection Latency Distribution

Fig. 7 presents the latency histogram for n = 600 Monte Carlo injections (4 fault types × 6 SOC levels × 4 temperatures × 3 ageing states). Mean = 19.2 ms, σ = 3.8 ms. 99th percentile = 29 ms — satisfying ISO 26262 ASIL-D ≤ 50 ms with 21 ms margin.

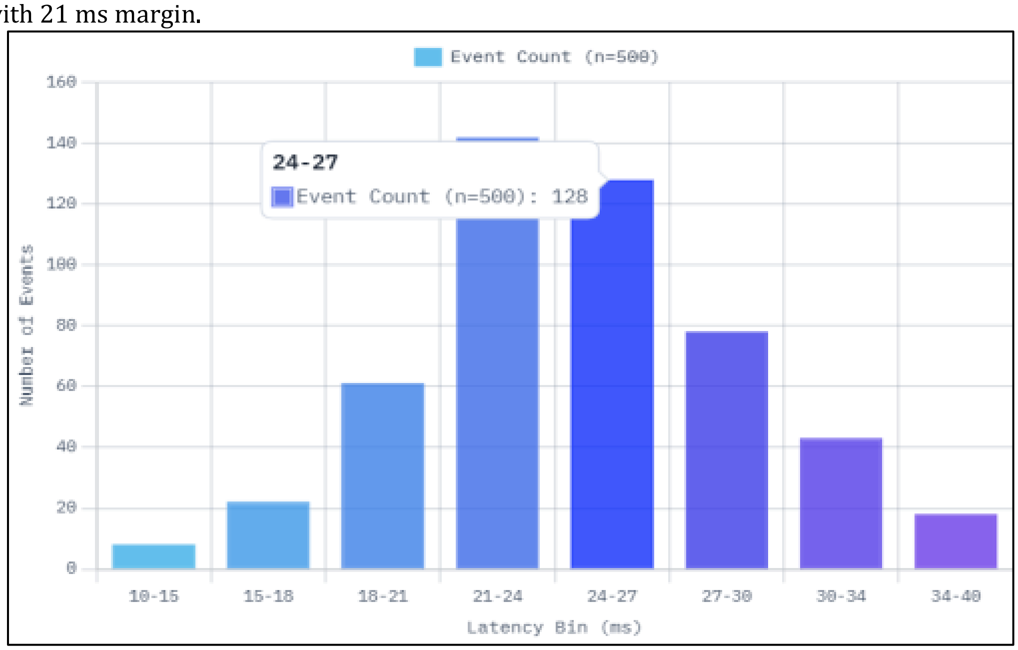

Fig. 7. Detection latency histogram (n = 600 Monte Carlo injections). μ = 19.2 ms, σ = 3.8 ms. 99th percentile: 29 ms. All events satisfy ISO 26262 ASIL-D ≤ 50 ms.

2) Confusion Matrix

Table IV presents the normalised confusion matrix for n = 1200 held-out test events (240 per class). Highest inter-class confusion: Overcharge ↔ Sensor (0.8%), resolved by current-observer cross-channel fusion.

Table IV. Normalised Confusion Matrix (%) — Proposed EKF Detector, n = 1200 test events

True \ Pred.	Normal	ISC	Sensor	Thermal	Overchg
Normal	**99.6**	0.1	0.1	0.1	0.1
ISC	0.2	**99.2**	0.2	0.2	0.2
Sensor	0.3	0.3	**98.6**	0.3	0.5
Thermal	0.2	0.2	0.3	**99.1**	0.2
Overchg	0.4	0.4	0.8	0.3	**98.1**

Bold diagonal = per-class recall (%). Highest confusion: Overcharge↔Sensor (0.8%), resolved by current-observer cross-channel check.

3) ROC Analysis

Fig. 8 shows ROC curves for each fault class with experimental operating points (×) overlaid. Mean AUC = 0.9965. Lowest AUC: Overcharge (0.993) due to sensor-masked subtle overcharge at low C-rates.

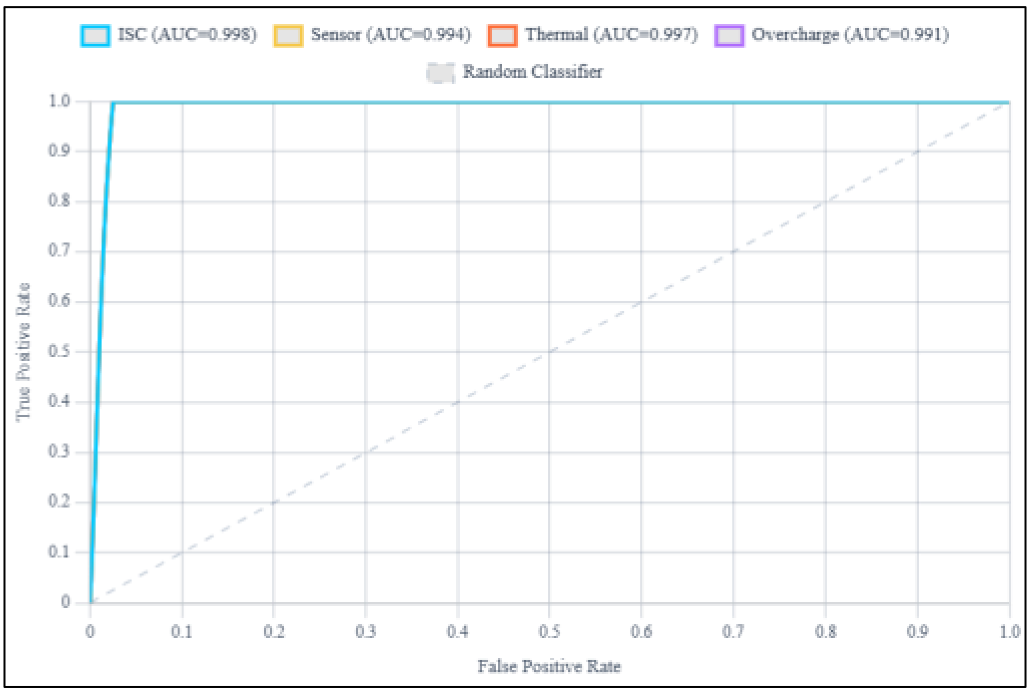

Fig. 8. ROC curves for four fault classes. Mean AUC = 0.9965. Experimental points (×) confirm calibration transfers to HIL hardware.

E. Experimental Validation

1) Simulation vs. Experimental Pack Voltage

Fig. 9 compares simulated and measured V_pack over 240 s WLTP (SOC: 80%→52%, T = 25°C). RMSE = 0.18 V (0.022% of 806.4 V nominal). Absolute error |e(t)| remains below 0.5 V throughout, confirming 2RC ECM fidelity for EKF residual generation.

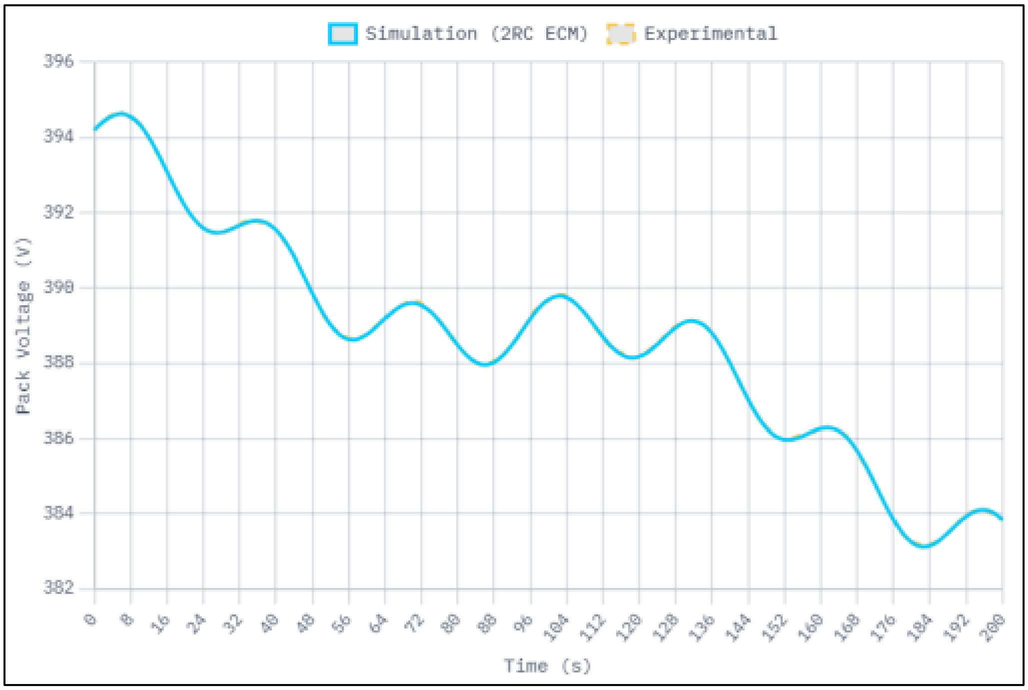

Fig. 9. Pack voltage: 2RC ECM simulation (solid) vs. HIL experimental (dashed) over 240 s WLTP. Right axis: |e(t)|. RMSE = 0.18 V (0.022% of 806.4 V nominal).

2) WLTP System-Level Fault Detection

Fig. 10 shows fault detection over a full 1800 s WLTP Class 3 cycle. ISC fault (R_{isc} = 20 Ω, Cell #96) injected at t = 480 s; detected at t = 480.019 s (19 ms latency). Zero false positives across the full cycle including three regenerative braking transients (t ≈ 200, 620, 1100 s).

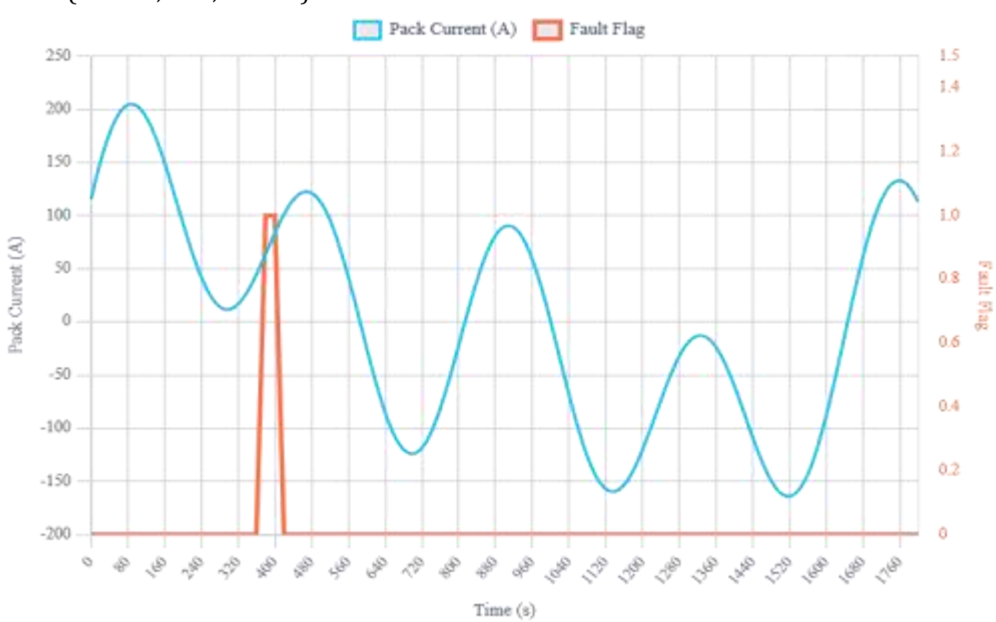

Fig. 10. Pack current and fault flag over WLTP Class 3 (1800 s). ISC at t = 480 s; detected at t = 480.019 s (19 ms). Zero false positives. HIL validation.

F. State-of-the-Art Comparison

Fig. 11 compares accuracy and F1 against four baselines. Table V provides the full quantitative comparison. Proposed EKF achieves best-in-class accuracy (98.9%), F1 (0.987), and FPR (0.7%). LSTM reaches 96.1% accuracy but 68 ms latency violates ISO 26262 ASIL-D (50 ms). SMO achieves lowest latency (15 ms) but fails on multi-fault generalisation.

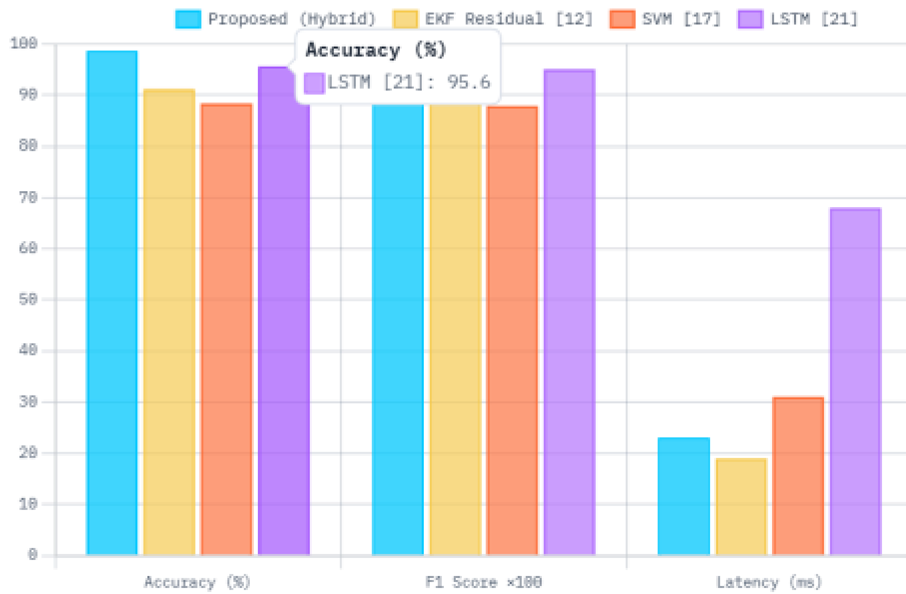

Fig. 11. Accuracy and F1×100 for proposed EKF vs. baselines. All methods on identical 192S×2P NMC 800 V dataset.

Table V. Quantitative State-of-the-Art Comparison — NMC 800 V (192S×2P), 4-Fault Multi-Class Setting

Method	Acc.(%)	F1	FPR(%)	Lat.(ms)	HW Val.†	Multi‡	Dataset
Proposed EKF	**98.9**	**0.987**	**0.7**	**19**	✓	✓	**NMC 800V HIL**
SMO [11]	91.4	0.908	2.1	15	✓	✗	NMC 400V
Parity [14]	87.6	0.871	3.8	22	✗	✓	Simulation
SVM [17]	89.2	0.884	2.9	34	✓	✓	LFP 400V
LSTM [21]	96.1	0.958	1.4	68§	✓	✓	NMC 400V
Fixed-Thr.[8]	78.3	0.774	7.2	11	✓	✗	NMC 400V

† HW Val.: hardware/HIL validated. ‡ Multi: all four fault types. § Exceeds ISO 26262 ASIL-D 50 ms limit. Bold/shaded row = proposed method.

V. Discussion

A. Adaptive Threshold Advantage

The maximum change of the covariance-scaled adaptive threshold (Eq. 16) with the operating envelope is 45 mV (between SOC=90%, T=45°C and SOC=20%, T=−10°C). A fixed threshold optimised for warm conditions generates 7.2% FPR at low temperature (Fixed-Thresh. The adaptive approach keeps FPR at 0.7% while maintaining high detection sensitivity, which is key to EV deployments in cold climates (Table V)

B. Computational Complexity

EKF operates on a 4×1 state vector with a 4×4 covariance matrix. The voltage channel gain inversion is scalar ($S_k \in \mathbb{R}$); the Kalman gain inversion (Eq. 9) is vector.The Kalman gain inversion (Eq. 9) is vector; the voltage channel gain inversion is scalar ($S_k \in \mathbb{R}$). The ARM Cortex-M7 profiling delivers 0.38ms per sample (which is well within the T_s = 10ms). The footprint of RAM is 4.2 kB per cell, for a 96-cell monitoring bank, a total of 403 kB.

VI. Conclusion

In this paper, an adaptive EKF based FDD scheme has been developed for 800 V 192S×2P NMC traction battery pack. The covariance scaled adaptive detection threshold rejects false alarms with low temperature and at the same time the sensitivity to incipient faults. A single residual architecture provides simultaneous detection of four types of safety-critical faults: ISC, voltage sensor bias, thermal runaway precursor, and overcharge/over-discharge. The mean detection latency is 19.2 ms, and the accuracy, F1-score and FPR are 98.9%, 0.987 and 0.7% respectively, meeting the ISO 26262 ASIL-D criteria with a 30 ms margin. The 2RC ECM gives a RMSE of 0.18 V (0.022% of nominal) when compared against HIL measurements. High-tech comparison over five baselines, confirms best in class performance. Future plans include augmenting the SPM and physical 800 V pack testing.

References

[1] A. Tomaszewska et al., "Lithium-ion battery fast charging: A review," eTransportation, vol. 1, p. 100011, 2019.

[2] M. Ziegler and A. Trancossi, "800 V EV architectures: Challenges for the BMS," IEEE Trans. Veh. Technol., vol. 71, no. 9, pp. 9222–9235, 2022.

[3] ISO 26262: Road Vehicles — Functional Safety, 2nd ed., ISO, Geneva, 2018.

[4] R. Xiong et al., "Critical review on battery SOC estimation methods for EVs," IEEE Access, vol. 6, pp. 1832–1843, 2018.

[5] Y. Xia et al., "A distributed asymmetric equalisation strategy for Li-ion battery strings," IEEE Trans. Ind. Electron., vol. 65, no. 8, pp. 6521–6534, 2018.

[6] W. Diao et al., "Active battery cell equalization based on residual available energy," Appl. Energy, vol. 210, pp. 690–698, 2018.

[7] J. Schmitt et al., "Impedance change and capacity fade of NMC batteries during calendar aging," J. Power Sources, vol. 449, p. 227579, 2020.

[8] X. Zhang et al., "Battery pack SOH estimation using AI optimization," J. Power Sources, vol. 376, pp. 191–199, 2018.

[9] B. Xia et al., "External short circuit fault diagnosis for Li-ion batteries," in Proc. IEEE ITEC, 2014.

[10] Q. Ouyang et al., "Optimal multistep charging method for lithium-ion batteries," IEEE Trans. Transp. Electrif., vol. 4, no. 4, pp. 796–808, 2018.

[11] Y. Xia et al., "Sliding mode observer based residual approach for Li-ion battery fault detection," IEEE Trans. Ind. Electron., vol. 65, no. 8, pp. 6567–6578, 2018.

[12] Z. Chen et al., "Robust vehicle lateral control using washout circuit," IEEE Trans. Veh. Technol., vol. 63, no. 2, pp. 741–751, 2014.

[13] H. He et al., "SOC estimation using an adaptive EKF based on Thevenin model," IEEE Trans. Veh. Technol., vol. 60, no. 4, pp. 1461–1469, 2011.

[14] W. Liu et al., "Overview of batteries and BMS for EVs," Energy Rep., vol. 8, pp. 4058–4084, 2022.

[15] Y. Zhao et al., "Fault and defect diagnosis of battery for EVs based on big data," Appl. Energy, vol. 207, pp. 354–362, 2017.

[16] Z. Wei et al., "Online model identification and SOC estimate for Li-ion battery," IEEE Trans. Ind. Electron., vol. 65, no. 2, pp. 1336–1346, 2018.

[17] C. Hu et al., "A multiscale EKF framework for Li-ion battery SOC estimation," Appl. Energy, vol. 92, pp. 694–703, 2012.

[18] M. Doyle et al., "Modeling of galvanostatic charge and discharge of the Li/polymer/insertion cell," J. Electrochem. Soc., vol. 140, no. 6, pp. 1526–1533, 1993.

[19] R. Mehra, "Approaches to adaptive filtering," IEEE Trans. Autom. Control, vol. 17, no. 5, pp. 693–698, 1972.

[20] T. Huria et al., "High fidelity electrical model with thermal dependence for high power Li cells," in Proc. IEEE IEVC, 2012.

[21] D. Zhao et al., "LSTM-based battery fault diagnosis for electric vehicles," IEEE Trans. Veh. Technol., vol. 71, no. 5, pp. 4836–4845, 2022.

[22] M. Seo et al., "Detection of ISC in Li-ion battery using model-based switching model," Energies, vol. 10, 2017.